Article

Not peer-reviewed version

Thermodynamic Properties and Shadow of a New Improved Schwarzschild Black Hole in the Infrared Limit

Celio Rodrigues Muniz * , Jonathan Alves Rebouças * , Francisco Bento Lustosa * ,
Francisco Tiago Barboza Sampaio , Leonardo Tavares de Oliveira

Posted Date: 26 February 2026

doi: 10.20944/preprints202602.1300.v1

Keywords: black holes; quantum gravity; thermodynamics

doi:10.20944/preprints202602.1300.v1

Article

Thermodynamic Properties and Shadow of a New Improved Schwarzschild Black Hole in the Infrared Limit

Celio Rodrigues Muniz [1,*], Jonathan Alves Rebouças [2,*], Francisco Bento Lustosa [1,*], Francisco Tiago Barboza Sampaio [1] and Leonardo Tavares de Oliveira [1]

[1] Universidade Estadual do Ceará (UECE), Faculdade de Educação, Ciências e Letras de Iguatu, 63500-000, Iguatu, CE, Brazil
[2] Instituto Federal de Educação Ciências e Tecnologia do Ceará (IFCE), Iguatu, Brazil
* Correspondence: celio.muniz@uece.br (C.R.M.); jonathan.reboucas@uece.br (J.A.R.); chico.lustosa@uece.br (F.B.L.)

Abstract

In this work we propose a modified Schwarzschild geometry inspired by the Asymptotic Safety approach to quantum gravity, in which the Newtonian coupling becomes a running quantity depending on the radial coordinate. We employ an infrared cutoff on the proper distance and obtain a new quantum-corrected black hole metric. We provide a thermodynamical analysis, first using standard methods and then proceeding to a geometrothermodynamical study of the phase space and to a topological analysis of phase transitions. We also calculate the grey-body factors of our solution, providing exact lower bounds in the quantum-corrected transmission coefficients. Finally, we present the shadow size and intensity profile of our solution, showing its consistency with current observational constraints.

Keywords: black holes; quantum gravity; thermodynamics

---

1. Introduction

The quest for a complete and consistent description of gravitational and quantum phenomena is one of the greatest challenges for Physics at the 21st century. In that quest, Black Holes (BHs) have become a standard theoretical tool to test the limits of known and new gravitational and quantum theories [1]. In particular, BH thermodynamics has become one of the main pathways to bridge the gap between classical and quantum phenomena and the derivation of their entropy in the context of AdS/CFT remains one of the most successful results coming from quantum gravity theories [2–6]. Beyond its theoretical potential, several direct and indirect observational windows into BH physics are now being studied through gamma and x-ray analysis [7], gravitational waves [8,9] and their shadow properties [10]. A remarkable result from gravitational wave observation has recently shown the validity of Hawking's area law [11], providing an explicit example of how observational results can constrain BH thermodynamics. BH shadow size has also become a common way to put constraints on different quantum and modified gravitational theories by comparing theoretical results with observations of M87 or Sagitarius A* [12–19].

One of the approaches to Quantum Gravity that has shown promise in the past decade is the Asymptotic Safety program originally proposed by Steven Weinberg (see [20] for original references on the first stages of the program), which relies only on advanced Quantum Field Theory methods and require only the assumption that the UV behavior of gravitation is controlled by an interacting fixed point of the gravitational renormalization group (RG) flow [21,22]. In this approach, all running couplings of matter fields approach a non-zero finite value, meaning that there will be a dependence of the couplings with energy up to this point. Standard Effective Field Theory applied to General Relativity also suggests that, whatever the UV behavior of gravity is, there should be a running of the Newton constant that translate to small corrections in the infrared limit [23]. Finding the exact UV

Preprints.org (www.preprints.org) | NOT PEER-REVIEWED | Posted: 26 February 2026 doi:10.20944/preprints202602.1300.v1

fixed point depends on non-perturbative renormalization techniques that have given strong support for the Asymptotic Safe Gravity (ASG) program but a complete phenomenological validation of the assumption might depend on directly observing the running of the gravitational constant that might leave distinct signatures only at very high energies. That is where black holes and cosmological scenarios come in to serve as test grounds for different theoretical results from the ASG program [20,24,25]. In order to do this, one has to obtain the specific running of the couplings from the RG flow equations and insert this into the action, equations of motion or solutions of the system under consideration. The couplings will now depend on the energy (or momentum k) scale of the fields and one still needs to find the correct infrared (IR) cutoff identification between momentum and the physical scale of the system [26]. This solutions are sometimes called ASG or RG-improved BH solutions and have been subject to several analysis in the recent years [20], showing their potential to provide indirect signatures of Quantum Gravity through corrections to Newton's constant [19,27].

In the ASG approach, the specific form of the running coupling will depend on the methods and parameters used to solve the RG flow equations. In a recent publication, Bonanno and collaborators showed how different parametrization and gauge choices lead to different running couplings using different regularization schemes on the proper time flor RG equation [28]. The result most commonly found in the literature was dubbed by the authors as "scheme C", while a new running coupling was found according to a new "scheme B" approach, which was subsequently applied to the dust ball case analyzed in [19]. RG improvement, as we already mentioned, will depend crucially on the IR cutoff scale; mapping that cutoff to a physical inverse length $\sim 1/d(r)$ yields coordinate-space effective couplings $G(r)$ and RG-improved metrics [21,25]. In [19] they chose to model an interior geometry with a standard FRW solution - as in the classical Oppenheimer-Snyder model for a dust collapse - and assumed a scaling of energy of the form $\epsilon \sim a^{-3}$, inputting the running of the coupling constant into the dynamical equations for the scale factor and then using matching conditions to a Schwarzschild-like exterior. Here we work with the exact scheme-B form of the dimension-full running Newton coupling in the IR limit, where we adopt the approximation for the proper-distance function $d(r) \approx r$ (valid for large r) and implement the standard IR cutoff in momentum as $k(r) \propto d(r)^{-}1$. This allows us to study the horizon physics of the BH taking into account a correction coming from ASG that will leave signatures at lower energies, without assuming an exact form for its UV behavior and without assumptions about the scale of the gravitational collapse that generated this black hole. In some sense, our approach is more conservative than the one presented in [19] and highlights how different ways of choosing an IR cutoff will lead to different physical features in general.

With the objective of studying this new solution from different perspectives we will employ different thermodynamical analysis in our work. The standard Hawking entropy and Gibbs's free energy are calculated for our modified solution, displaying interesting features that indicate the presence of a remnant after evaporation. We also present a geometrothermodynamical analysis, which discusses the geometry of the phase space of thermodynamic variables and can also be used to study phase transitions from a semi-classical perspective. Our approach will be based on a recent work by S. H. Hendi and collaborators who introduced a new thermodynamical metric that correctly finds divergencies - phase transitions - from the corresponding gravitational system through the metric in phase space [29]. This method has been gaining interest in the recent years and has been applied to multiple BH solutions [30,31]. We will also employ a topological analysis of the thermodynamics of our system, using the generalized off-shell free energy proposed by R. Mann and collaborators [32]. The triple analysis of thermodynamics confirms the robustness of the results found in the IR limit and provides a complete picture of the possible phase transitions of our solution.

Beyond the thermodynamical analysis, another valuable tool to study observational signatures of modified BH solutions are the grey-body factors, that describe the partial transmission of quantum fields through curved spacetime and can be used to determine the intensity and spectrum of Hawking radiation [19,27,33–36]. This factors might also be of use to study ring-down features of gravitational waves that cannot be accurately model with quasinormalmodes [37]. Finally, a key feature of any BH solution is its shadow size, determined by the radius of the photons sphere around the horizon [10]. We provide further analysis of the shadow using its intensity profile, that can gauge how light piles-up around the horizon and can be affected by the modified metric structure [16,17].

The presented combined thermodynamical and optical analysis provides a complete picture of how a simple infrared modification can impact the structure and behavior of our BH solution. The ASG approach provides a clear and consistent path to find corrections from quantum effects in the UV regime that translate in some form of modification of the physics in the IR. The challenge remains to find the complete connection between the two regimes. Our analysis highlights how IR effects can carry signatures of quantum gravity to known BH observables and serve to phenomenologically test this approach further.

The paper is organized as follows. In Section 2 we briefely present the running gravitational coupling obtained using scheme B of Bonanno and collaborators [19,28], and present the basic geometrical properties of our solution, also calculating the Kretschmann scalar. In Section 3 we start our thermodynamical analysis by calculating Hawking temperature, entropy and heat capacity. In Section 4 we study the geometrothermodynamical behavior of our solution, according to the proposed methods of [29]. In Section 5 we present the topological analysis using stram plots of the vector fields constructed from the generalized Gibbs free energy proposed by [32]. In Section 6 we calculate and analyze the grey-body factors, showing how quantum corrections modified its behavior. In Section 7 we present the shadow radius and its corresponding intensity profiles. In the last section we discuss our conclusions.

2. The New Improved Black Hole Solution and its Geometric Properties

Initially, according to [19,28], we take the scheme-B of improvement expression for the Newton coupling in the limit $\Lambda_0 = 0$. Denoting the IR Newton constant by G_0 and the dimensionless fixed-point value by g_*, the running coupling reads

$$G^{(B)}(\Lambda)\Big|_{\Lambda_0=0} = \frac{G_0}{\dfrac{\Lambda^2}{2}\left(\dfrac{G_0}{g_*}\right) + \sqrt{1 + \dfrac{1}{4}\Lambda^4\left(\dfrac{G_0}{g_*}\right)^2}} . \tag{1}$$

Following the interpolating prescription of Bonanno & Reuter [25], we identify the RG cutoff with an inverse proper-like distance:

$$\Lambda(r)\left(\frac{G_0}{g_*}\right)^{1/2} = \frac{\xi}{d(r)}, \tag{2}$$

where ξ is a cutoff distance scale and γ is the interpolation parameter. In the IR approximation, where $d(r) \approx r$, the scheme-B yields

$$G^{(B)}(r) = \frac{G_0}{\dfrac{\xi^2}{2r^2} + \sqrt{1 + \dfrac{\xi^4}{4r^4}}}. \tag{3}$$

Consequently, in the scheme-C presented in [19], it follows that

$$G^{(C)}(r) = \frac{G_0}{1 + \dfrac{\xi^2}{r^2}}. \tag{4}$$

Replacing the classical Newtonian constant G_0 in the Schwarzschild solution by the running coupling (3), we obtain the black hole metric, written as

$$ds^2 = -f(r)\, dt^2 + f(r)^{-1}\, dr^2 + r^2 d\Omega^2, \tag{5}$$

with the lapse function in the scheme-B

$$f(r) = 1 - \frac{2M\,G(r)}{r} = 1 - \frac{4Mr}{\xi^2 + \sqrt{4r^4 + \xi^4}}. \tag{6}$$

And the lapse function in the scheme-C takes the form

$$f^{(C)}(r) = 1 - \frac{2Mr}{r^2 + \xi^2}. \tag{7}$$

These expressions reproduce the standard Schwarzschild form in the limit $\xi \to 0$ or $r \to \infty$, while for finite ξ it regularizes the metric function near $r = 0$. In the following sections we analyze its curvature invariants, horizons, and thermodynamic properties.

An analysis of Equation (6) allows us to identify the horizons through the real and positive roots of f. By varying the parameters M and ξ, we observe the formation of at most two event horizons, as shown in Figure 1. In the left panel, when varying the mass M while keeping the cutoff scale parameter fixed at $\xi = 1$, the horizons begin to exist for $M \geq 0.8$. In the right panel, with $M = 1$ fixed, the event horizons for schemes B and C are shown. Scheme-C is represented by the dashed curve for $\xi = 0.60$, while the remaining curves correspond to Scheme-B, for which the horizons appear for $\xi \geq 1.24$.

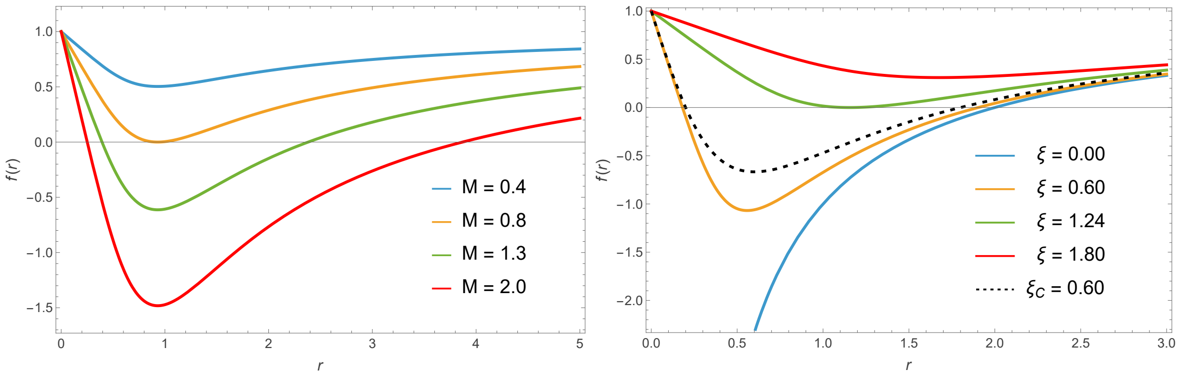

Figure 1. Left panel: varying the mass M, with $\xi = 1$. Right panel: varying the cutoff scale parameter ξ, with $M = 1$, where the dashed curve represents the regularization function of Scheme-C.

We now proceed with the analysis of the curvature properties of the spacetime under consideration, focusing on the Kretschmann scalar $K(r)$. This invariant, which measures the magnitude of the Riemann tensor, is given by

$$K(r) = R_{\mu\nu\sigma\lambda}R^{\mu\nu\sigma\lambda} = \left(f''(r)\right)^2 + \frac{4}{r^2}\left(f'(r)\right)^2 + \frac{4}{r^4}\left(1 - f(r)\right)^2. \tag{8}$$

From the asymptotic expansion of (8), the dominant infrared contribution to the Kretschmann scalar K, takes the form

$$K(r) = \frac{48\,M^2}{r^6} + O(r^{-7}), \tag{9}$$

with the leading term of K being identical to the Schwarzschild behavior, consistent with $G(r) \to G_0$ as $r \to \infty$. On the other hand, the expansion in the limit $r \to 0$ yields

$$K = \frac{32M^2}{\xi^4 r^2} + \mathcal{O}(r), \tag{10}$$

which indicates that the solution is singular. Since our analysis is restricted to the IR regime, the presence of such a singularity at the center is a natural feature of this improved Schwarzschild solution. In practice, however, this region is excluded from our analysis because quantum effects at the Planck scale are expected to dominate there and can only be consistently described within the fully improved solution. Nevertheless, in our approach, quantum effects may still be relevant at the scale of the event horizon and can therefore manifest themselves through modifications of its thermodynamic properties, which will be the subject of the next section.

3. Thermodynamics

We proceed with the study of the new improved Schwarzschild black hole by analyzing its thermodynamic properties, which are derived from the metric function (6). Initially, considering the condition $f(r_h) = 0$, the mass M as a function of the horizon radius r_h is

$$M(r_h, \xi) = \frac{\xi^2 + \sqrt{4r_h^4 + \xi^4}}{4r_h}, \tag{11}$$

where the standard Schwarzschild mass is recovered in the appropriate limit $\xi \to 0$.

To advance the thermodynamic analysis, it is necessary to distinguish between the internal and external horizons, which is determined by examining how the mass depends on the horizon radius. The mass function $M(r_h)$ exhibits a minimum M_{ext} at $r_h = r_h^{\text{min}} = (3/4)^{1/4}\xi$, corresponding to the extremal configuration where the inner and outer horizons coincide ($r_+ = r_- = r_h^{\text{min}}$). Consequently, the thermodynamic analysis must be restricted to the parameter ranges that yielding a real outer horizon, i.e., $M \geq M_{\text{ext}}$ (or equivalently $r_+ \geq r_h^{\text{min}}$).

In Figure 2, we present the relation between the black hole mass and the radius r_h for different values of the parameter ξ. Since only the branch of the curve with $r_h \geq r_h^{\text{min}}$ corresponds to a physical event horizon, for $\xi = 0.6$ this limit occurs at $r_h^{\text{min}} \approx 0.55$.

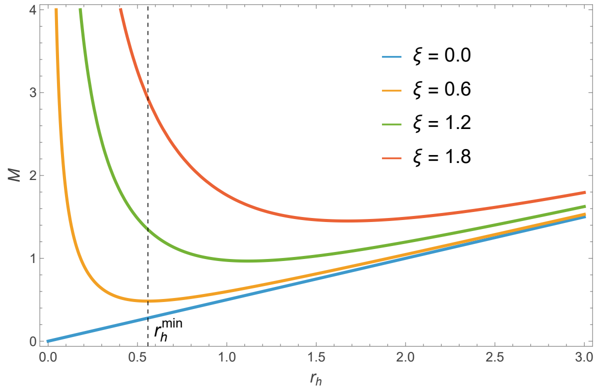

Figure 2. The black hole mass as a function of the event horizon radius r_h, for different values of the cutoff scale parameter ξ, with $r_h^{min} \approx 0.55$ for $\xi = 0.6$.

For the Hawking temperature, obtained from the surface gravity at the event horizon, i.e., $T_H = f'(r_h)/(4\pi)$, it follows in this model that

$$T_H(r_h, \xi) = \frac{1}{4\pi r_h}\left(1 - \frac{2\xi^2}{\sqrt{4r_h^4 + \xi^4}}\right). \tag{12}$$

Furthermore, in the regularization scheme-C, the Hawking temperature takes the form

$$T_H^{(C)}(r_h, \xi) = \frac{1}{4\pi r_h}\left(\frac{r_h^2 - \xi^2}{r_h^2 + \xi^2}\right), \tag{13}$$

where, in the limit $\xi \to 0$, both expressions reduce to the temperature of a Schwarzschild black hole, namely, $T_{\text{Schw}} = (4\pi r_h)^{-1}$.

Figure 3 shows the Hawking temperature as a function of the event horizon radius, for different values of the parameter ξ (Scheme-B) and a dashed curve representing the regularization scheme-C. The temperature increases as r_H decreases, reaches a maximum, and then drops to zero, indicating a phase transition and the formation of a remnant when $T_H = 0$. These remnant radii, for schemes B and C, are given by $r^B_{rem} = (3/4)^{1/4}\xi$ and $r^C_{rem} = \xi$, respectively.

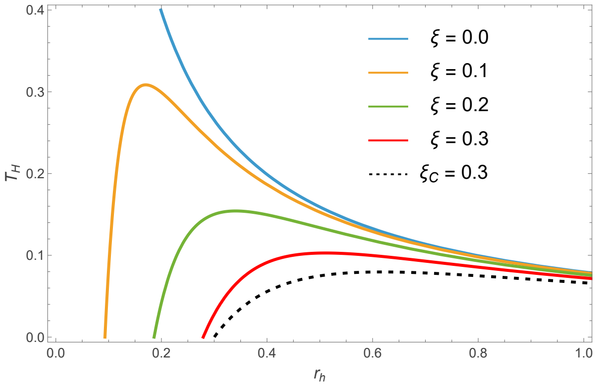

Figure 3. Hawking temperature as a function of the event horizon radius r_h, for different values of the parameter ξ. A dashed curve representing the regularization scheme-C.

The thermodynamic properties of our black hole solution are further explored by examining the Bekenstein-Hawking entropy S. By integrating the first law of black hole thermodynamics, $dS = T_H^{-1} dM$, where $M(r_h)$ and $T_H(r_h)$ are given by Eqs. (11) and (12), respectively, we derive the analytical expression for the entropy:

$$S(r_h, \xi) = \pi r_h^2 + \frac{\pi \xi^2}{2} \ln\left(\frac{2r_h^2 + \sqrt{4r_h^4 + \xi^4}}{\xi^2}\right). \tag{14}$$

This result reveals that the entropy is composed of the classical area law, $S_{BH} = A/4 = \pi r_h^2$, supplemented by a non-trivial logarithmic correction term regulated by the scale ξ. Such logarithmic dependencies are a universal hallmark of quantum-corrected geometries, often arising from microstate counting as a consequence of the renormalization group improvement in the ASG framework. In the limit $\xi \to 0$, the classical Schwarzschild area relation is exactly recovered. The presence of this quantum-inspired term is crucial for the thermodynamic stability of the system, particularly in the final stages of evaporation, where it supports the existence of a cold remnant.

In order to emphasize the robustness of the black hole in the Scheme-B, it is instructive to compare its entropy with that obtained from a simpler renormalization group improvement, namely, Scheme-C. For the latter, the first law leads to a simpler logarithmic correction of the form $S^{(C)} = \pi r_h^2 + \pi\xi^2 \ln(r_h^2)$. While both models incorporate quantum-inspired corrections, the logarithmic term in the black hole metric exhibits a more intricate dependence on the non-local scale ξ, as seen in the argument of the logarithm in Equation (14). This structural difference ensures a smoother thermodynamic transition as the black hole approaches the higher energy scales. Furthermore, as previously discussed, the black hole metric provides a more stable framework for the cold remnant phase, consistent with the tighter constraints imposed by recent shadow observations from M87* and Sgr A*, as we will see, where the Scheme-B shows superior phenomenological agreement compared to the more abrupt corrections of Scheme-C.

Regarding the heat capacity, $C = \dfrac{dM}{dT_H} = \dfrac{dM/dr_h}{dT_H/dr_h}$, of the new improved Schwarzschild black hole, it follows from

$$C(r_h,\xi) = -\frac{\pi\left(4r_h^4+\xi^4\right)\left(4r_h^4-\xi^4-\xi^2\sqrt{4r_h^4+\xi^4}\right)}{4r_h^4\left(\sqrt{4r_h^4+\xi^4}-6\xi^2\right)+\xi^4\left(\sqrt{4r_h^4+\xi^4}-2\xi^2\right)}. \tag{15}$$

For the heat capacity given by Scheme-C, it follows that

$$C^{(C)}(r_h,\xi) = -\frac{2\pi(r_h^2-\xi^2)\,(r_h^2+\xi^2)^2}{r_h^4-4r_h^2\xi^2-\xi^4}, \tag{16}$$

where the heat capacity of the Schwarzschild black hole, $C_{\mathrm{Schw}} = -2\pi r_h^2$, is recovered when $\xi \to 0$. The Figure 4 shows the behavior of the heat capacity as a function of the event horizon radius for different values of the cutoff scale parameter ξ, with the dashed curve representing the heat capacity in Scheme-C for $\xi = 0.6$.

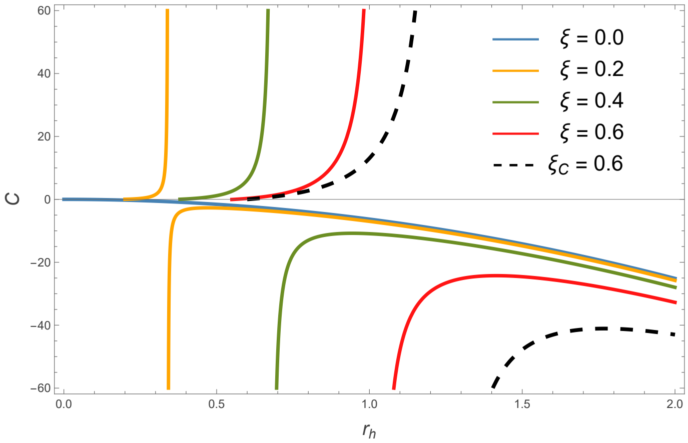

Figure 4. Heat capacity as a function of the event horizon radius r_h. The dashed curve represents the regularization solution of Scheme-C. With the blue curve indicating the Schwarzschild black hole.

To complete the usual thermodynamic characterization of the enhanced Schwarzschild black hole in the IR limit, we analyze the Gibbs Free Energy, henceforth (G). In the canonical ensemble, this potential determines the global stability of the system. The Gibbs free energy is defined by the Legendre transformation of mass with respect to entropy, given by

$$G(r_h,\xi) = M(r_h,\xi) - T_H(r_h,\xi)S(r_h,\xi) \tag{17}$$

To obtain the expression for Scheme-B (our proposed solution), it is necessary to combine the thermodynamic functions derived previously. We use the mass $M(r_h,\xi)$ defined by Equation (11), which represents the total energy of the system corrected by the scale ξ. We incorporate the Hawking temperature $T_H(r_h,\xi)$ from Equation (12), obtained via surface gravity, and the entropy $S(r_h,\xi)$ from Equation (14), which includes the logarithmic correction. To simplify the representation, we define the auxiliary function $\Delta \equiv \sqrt{4r_h^4+\xi^4}$. Thus, the corrected entropy Equation (14) can be written compactly in terms of the inverse hyperbolic sine:

$$S(r_h,\xi)^{(C)} = \pi r_h^2 + \frac{\pi\xi^2}{2}\operatorname{arcsinh}\left(\frac{2r_h^2}{\xi^2}\right) \tag{18}$$

Substituting the mass $M = \frac{\Delta+\xi^2}{4r_h}$ and the temperature $T_H = \frac{1}{4\pi r_h}\left(1 - \frac{2\xi^2}{\Delta}\right)$ into the definition of the potential, the Gibbs free energy for Scheme-B takes the following form:

$$G(r_h, \xi) = \frac{1}{4r_h}\left[\Delta + \xi^2 - \left(1 - \frac{2\xi^2}{\Delta}\right)\left(r_h^2 + \frac{\xi^2}{2}\text{arcsinh}\left(\frac{2r_h^2}{\xi^2}\right)\right)\right] \tag{19}$$

For comparative purposes, we analyze Scheme-C, using the lapse function from Equation (7). With the mass $M^{(C)} = (r_h^2 + \xi^2)/(2r_h)$, the temperature from Equation (13), and the simplified entropy, the potential for the reference model is given by:

$$G^{(C)}(r_h, \xi) = \frac{r_h^2 + \xi^2}{2r_h} - \left[\frac{1}{4\pi r_h}\left(\frac{r_h^2 - \xi^2}{r_h^2 + \xi^2}\right)\right]\left[\pi r_h^2 + \pi\xi^2 \ln(r_h^2)\right] \tag{20}$$

In the classical limit $\xi \to 0$, both schemes recover the Schwarzschild behavior, $G_{Schw} = r_h/4 = \frac{M}{2}$, where the black hole is thermodynamically unstable in vacuum.

The Analysis reveals that, for our model, G remains positive and reaches a finite value at the radius of the stable remnant, $r_{rem} = (3/4)^{1/4}\xi$. Since the temperature T_H vanishes at this point, the thermal interaction term $T_H S$ disappears, and the value of G converges exactly to the mass of the remnant: $G(r_{rem}, \xi) = M(r_{rem}, \xi) > 0$. This behavior confirms that the remnant is a stable final state, halting evaporation.

The comparison between the two models for $\xi = 0.6$ shows that our proposal provides a smoother thermodynamic transition. While Scheme-C exhibits more abrupt variations due to the logarithmic correction. Thus, the non-linear structure of our solution ensures a continuous regularization of the thermal phases. This stability is consistent with observations of black hole shadows and reinforces the phenomenological viability of the model within the framework of ASG. To illustrate that behavior, we have shown in Figure 5 that the Gibbs free energy remains finite throughout the physical domain. Each curve starts at a different lower bound because the allowed range is $r_h \geq r_{\text{rem}} = (3/4)^{1/4}\xi$, so increasing ξ shifts the onset of the plot to larger radii. As r_h increases, all Scheme-B curves approach the same asymptotic trend and progressively converge toward the $\xi \to 0$ (Schwarzschild) behavior, indicating that the quantum-inspired corrections become subleading at large radii. For comparison, the dashed curve (Scheme-C) exhibits a systematically higher Gibbs free energy and a milder variation over the plotted range, reflecting the different functional dependence of the running coupling in that prescription. In the limit $\xi \to 0$, the curve becomes linear, consistently reproducing the Schwarzschild result discussed above.

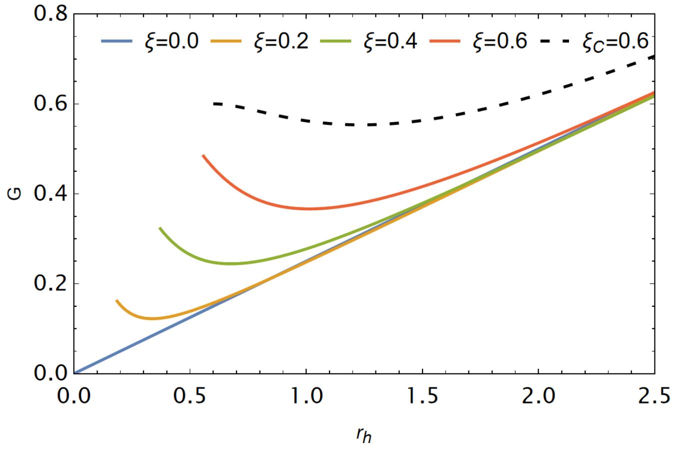

Figure 5. Gibbs free energy G as a function of the event horizon radius r_h for different values of the cutoff scale parameter ξ in Scheme-B. The dashed curve represents the reference Scheme-C for $\xi = 0.6$.

4. Thermodynamic Geometry

In this section, we investigate the thermodynamic phase structure of the black hole using the Hendi–Panahiyan–Eslam Panah–Momennia (HPEM) thermodynamic geometry formalism [29]. Our analysis is performed in the extended phase space, where the parameter ξ is promoted to an independent thermodynamic charge. Consequently, the black hole mass M assumes the role of the system's enthalpy, and the first law of thermodynamics is extended to include a work term associated with the variation of the infrared scale from ASG. The differential form of the extended first law is expressed as $dM = T_H dS + \Psi d\xi$, where T_H is the Hawking temperature and Ψ represents the thermodynamic potential conjugate to ξ. This formulation ensures internal consistency between the quantum corrections in the metric and the laws of thermodynamics, allowing the stability of the system to be analyzed within a two-dimensional phase space. Based on the mass expression for Scheme-B, the conjugate potential is calculated as:

$$\Psi = \left(\frac{\partial M}{\partial \xi}\right)_S = \frac{\xi}{2r_h}\left(1 + \frac{\xi^2}{\sqrt{4r_h^4 + \xi^4}}\right). \tag{21}$$

In this extended phase space, the mass is regarded as a function of the entropy and the charge ξ, namely $M = M(S, \xi)$, implicitly defined through the relation between S and the horizon radius r_h. Following the HPEM prescription, the thermodynamic metric on the space of extensive variables (S, ξ) is defined as

$$g^{\mathrm{HPEM}} = S\left(\frac{\partial M}{\partial S}\right)\left(\frac{\partial^2 M}{\partial \xi^2}\right)^{-3}\left(-\frac{\partial^2 M}{\partial S^2}\, dS^2 + \frac{\partial^2 M}{\partial \xi^2}\, d\xi^2\right), \tag{22}$$

which is constructed to ensure that curvature singularities arise exclusively from genuine thermodynamic instabilities, avoiding unphysical divergences. Thus, for a two–dimensional diagonal metric of the form

$$ds^2 = A(S, \xi)\, dS^2 + B(S, \xi)\, d\xi^2, \tag{23}$$

with $A(S, \xi) = -\frac{S M_S M_{SS}}{M_{\xi\xi}^3}$ and $B(S, \xi) = \frac{S M_S}{M_{\xi\xi}^2}$, the Ricci scalar can be computed analytically. After substituting the HPEM metric components and simplifying, the curvature scalar assumes the generic structure

$$\begin{aligned} R^{HPEM}(r_h, \xi) = \frac{1}{2AB}\Bigg[&\frac{(\partial_\xi A)(\partial_\xi B)}{AB} + \frac{(\partial_\xi A)^2}{A^2} - \frac{2\partial_\xi^2 A}{A} + \frac{(\partial_{r_h} A)(\partial_{r_h} B)}{(\partial_{r_h} S)^2 AB} \\ &+ \frac{(\partial_{r_h} B)^2}{(\partial_{r_h} S)^2 B^2} - \frac{2}{B\partial_{r_h} S}\partial_{r_h}\left(\frac{\partial_{r_h} B}{\partial_{r_h} S}\right)\Bigg] \end{aligned} \tag{24}$$

In terms of the thermodynamic variables (S,ξ), the scalar is

$$R^{\mathrm{HPEM}} = \frac{\mathcal{N}(S, \xi)}{\left(\frac{\partial^2 M}{\partial S^2}\right)^2 \left(\frac{\partial^2 M}{\partial \xi^2}\right)^3}, \tag{25}$$

where $\mathcal{N}(S, \xi)$ is a regular function of the thermodynamic variables. Crucially, the numerator does not introduce additional singularities. Therefore, divergences of the HPEM Ricci scalar occur if and only if

$$\frac{\partial^2 M}{\partial S^2} = \frac{\partial T_H}{\partial S} = 0, \tag{26}$$

which coincides exactly with the divergence points of the heat capacity. This confirms that the thermodynamic geometry consistently captures the phase transition structure of the black hole when the corrected entropy is employed.

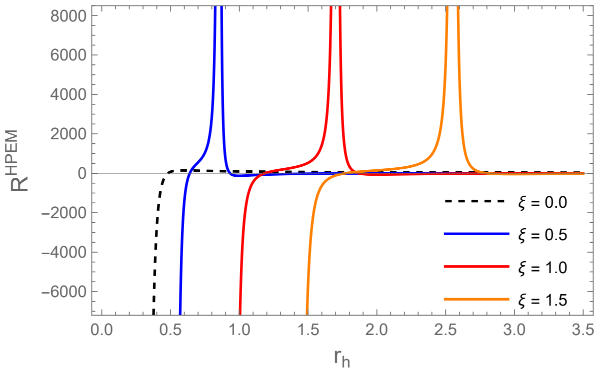

Figure 6. Behavior of the thermodynamic curvature scalar R^{HPEM} as a function of the horizon radius r_h for different values of the ASG parameter ξ in Scheme-B, with each curve initiated at the physical limit of the remnant radius r_{rem}.

The thermodynamic curvature scalar R^{HPEM}, as shown in Figure 6, exhibits divergences that precisely map the critical points of the improved Schwarzschild black hole. The latter is incidentally depicted by the dashed curve. The first singularity occurs at the remnant radius $r_{rem} = (3/4)^{1/4}\xi$, where the Hawking temperature vanishes, indicating the limit of validity for the classical thermodynamic description and the stabilization of the system into a final quantum-gravity state. A second divergence emerges for larger values of r_h, coinciding with the point where the heat capacity becomes infinite, signaling a second-order phase transition between thermodynamically stable and unstable configurations. This geometric representation in the phase space confirms that the cutoff parameter ξ acts as a regulator that introduces new correlation scales and equilibrium points absent in the classical Schwarzschild solution.

5. Thermodynamic Topology

Motivated by the topological interpretation proposed in Ref. [32], we analyze the present RG-improved Schwarzschild model by treating its thermodynamic states as defect structures in an off-shell free-energy landscape. The starting point is the off-shell generalized Gibbs free energy

$$\mathcal{F}^{(i)}(r_h,\xi;\tau) = M^{(i)}(r_h,\xi) - \frac{S^{(i)}(r_h,\xi)}{\tau}, \tag{27}$$

where $\tau > 0$ is an external control parameter and $i \in \{B, C\}$ labels the regularization prescription (we adopted here the B label for pedagogical distinction). In our case, the thermodynamic functions are those derived in Sec. 3: for Scheme–B, $M^{(B)}(r_h,\xi)$ and $S^{(B)}(r_h,\xi)$ are given by Eqs. (11) and (14), while for Scheme–C we use $M^{(C)}(r_h,\xi) = (r_h^2 + \xi^2)/(2r_h)$ and $S^{(C)}(r_h,\xi) = \pi r_h^2 + \pi\xi^2 \ln(r_h^2)$. The physically relevant domain is restricted by the remnant radii, namely $r_h \geq r^B_{\rm rem} = (3/4)^{1/4}\xi$ and $r_h \geq r^C_{\rm rem} = \xi$.

To construct the phase-space flow, we introduce an auxiliary angle $\Theta \in (0,\pi)$ and define the two-dimensional vector field [32]

$$\vec{\phi}^{(i)} = \left(\phi^1, \phi^2\right) = \left(\frac{\partial \mathcal{F}^{(i)}}{\partial r_h}, -\cot\Theta \csc\Theta\right). \tag{28}$$

The zeros of $\vec{\phi}^{(i)}$ are determined by the simultaneous conditions $\Theta = \pi/2$ and

$$\left.\frac{\partial \mathcal{F}^{(i)}}{\partial r_h}\right|_{\tau} = 0 \quad \Longleftrightarrow \quad \frac{\partial M^{(i)}}{\partial r_h} - \frac{1}{\tau}\frac{\partial S^{(i)}}{\partial r_h} = 0 \quad \Longrightarrow \quad \tau = \frac{\partial S^{(i)}/\partial r_h}{\partial M^{(i)}/\partial r_h} = \frac{1}{T_H^{(i)}(r_h,\xi)}, \tag{29}$$

where the last equality follows from the first law $dM = T_H\, dS$ already employed to obtain $S(r_h,\xi)$ in Sec. 3. Therefore, the defect points in the (r_h,Θ) plane are in one-to-one correspondence with the on-shell relation $\tau = \tau_H(r_h) \equiv 1/T_H(r_h,\xi)$, with $T_H^{(B)}$ and $T_H^{(C)}$ given by Eqs. (12) and (13).

Following Ref. [32], we associate to $\vec{\phi}^{(i)}$ the topological current

$$j^{\mu} = \frac{1}{2\pi}\,\epsilon^{\mu\nu\rho}\epsilon_{ab}\,\partial_{\nu}n^{a}\,\partial_{\rho}n^{b}, \tag{30}$$

where $\mu, \nu, \rho = 0, 1, 2$ and $a, b = 1, 2$. The unit vector $\vec{n}$ is defined as

$$n^1 = \frac{\phi^1}{\phi}, \qquad n^2 = \frac{\phi^2}{\phi}, \qquad \phi = |\vec{\phi}|. \tag{31}$$

The current (30) is identically conserved and is non-vanishing only at the zeros of $\vec{\phi}^{(i)}$ [32]. In particular,

$$j^0 = \frac{1}{\pi}\Big(\partial_1 n^1 \partial_2 n^2 - \partial_2 n^1 \partial_1 n^2\Big), \tag{32}$$

where we identify $(x^1, x^2) \equiv (r_h, \Theta)$. In regions where $\phi \neq 0$ and ϕ^a are smooth, one may rewrite

$$j^0 = \frac{1}{\pi}(\partial_1 Q - \partial_2 P), \qquad Q = n^1 \partial_2 n^2, \qquad P = n^1 \partial_1 n^2. \tag{33}$$

Hence, for a domain D free of zeros of $\vec{\phi}^{(i)}$, Green's theorem yields

$$0 = \int_D j^0\, d^2x = \frac{1}{\pi}\int_D (\partial_1 Q - \partial_2 P)\, d^2x = \frac{1}{\pi}\oint_{\Sigma} (P\, dx^1 + Q\, dx^2) = \frac{1}{\pi}\oint_{\Sigma} n^1\, dn^2.$$

For a closed contour C enclosing all zeros of $\vec{\phi}^{(i)}$, the total topological number is defined by

$$W = \frac{1}{\pi}\oint_C n^1\, dn^2 = \frac{1}{\pi}\sum_{k=1}^{N}\oint_{c_k} n^1\, dn^2, \tag{34}$$

where each c_k is a small loop surrounding a single defect.

In the present model, the remnant condition $T_H(r_{\rm rem}) = 0$ implies $\tau_H \to \infty$ at the beginning of the physical domain, so the topological analysis is restricted to $r_h \geq r_{\rm rem}$. This behavior is explicitly illustrated in Figure 7: in the bottom panels, $\tau_H(r_h) = 1/T_H(r_h)$ starts at infinity, decreases until reaching a local minimum $\tau_{\rm min}$, and then increases again. Hence, for any fixed $\tau > \tau_{\rm min}$ (dashed lines in the bottom panels), the equation $\tau = \tau_H(r_h)$ admits two solutions, which appear as two zero points of the vector field $\vec{\phi}$ at $\Theta = \pi/2$ in the corresponding stream plots (top panels). These two defects represent the two thermodynamic branches separated by the critical point already signaled by the divergence of the heat capacity in Figure 4. Comparing Scheme–B and Scheme–C at the same ξ, the same defect pattern is preserved, but the positions of the zeros and the width of the stable window shift because $G(r)$ modifies T_H and S differently in each prescription; in particular, Scheme–B yields a smoother deformation of the Schwarzschild thermodynamic landscape, whereas Scheme–C produces a more displaced defect structure for the same cutoff scale.

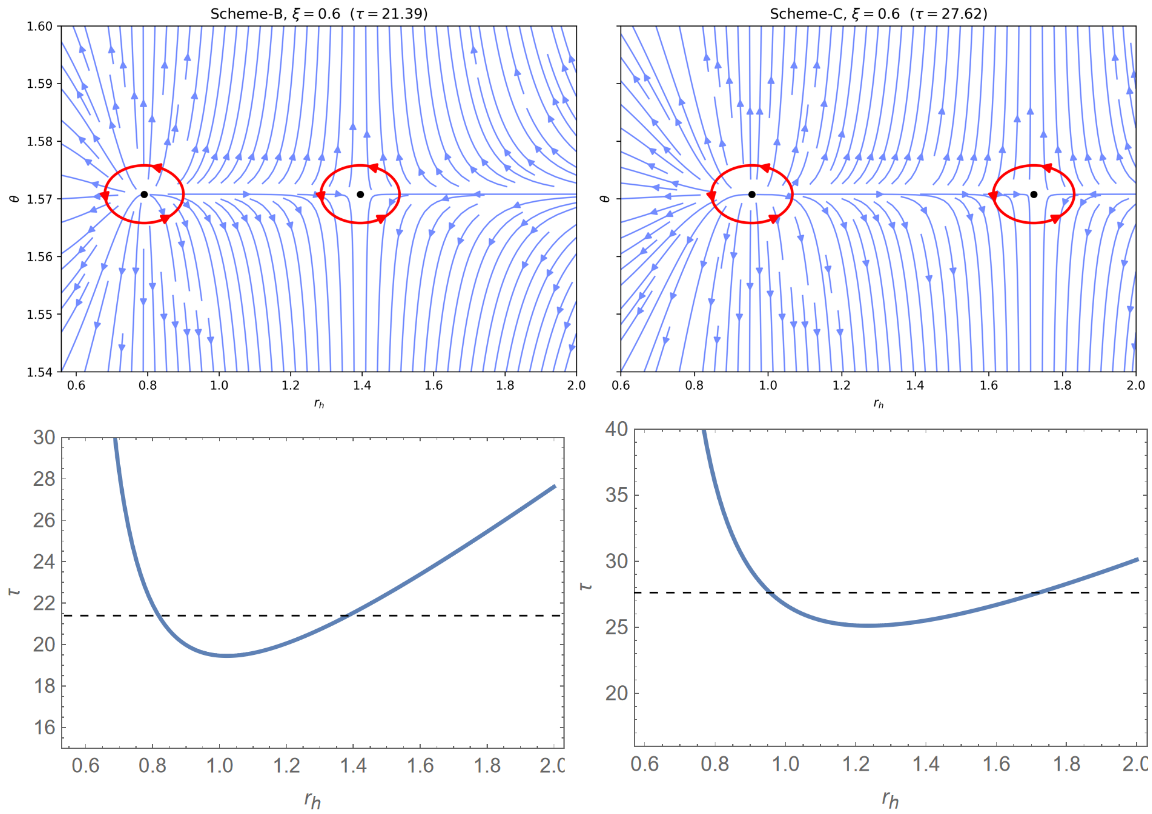

Figure 7. Top panels: Stream plot of the phase-space vector field $\vec{\phi}(r_h, \Theta)$ for the RG-improved Schwarzschild black hole with $\xi = 0.6$. Left: Scheme–B. Right: Scheme–C. The zeros are highlighted by the black points (red circles). Bottom panels: Corresponding $\tau_H(r_h) = 1/T_H(r_h)$ profiles; the dashed horizontal line indicates the fixed off-shell parameter τ used in the top panels.

6. Grey-Body Factors

The effective potential for a massless scalar field, as discussed in [34–36], is given by

$$V(r_*) = f\left[\frac{l\,(l+1)}{r^2} + \frac{f'}{r}\right], \tag{35}$$

where r_* is the tortoise coordinate, defined as $\dfrac{dr_*}{dr} = \dfrac{1}{f}$, and l is the angular quantum number.

From the effective potential, we determine the grey-body factors, which measure the deviation of the radiation spectrum emitted by a black hole from that of a perfect black body [36]. Thus, according to [35,36], a lower bound for the quantum transmission coefficients through the potential barrier, in other words, the grey-body factors, is given in the form

$$T \geq \mathrm{sech}^2\left(\frac{1}{2\omega}\int_{-\infty}^{\infty} |V|\, dr_*\right). \tag{36}$$

Using Equation (35) in expression (36), and considering that, in our case, there is no cosmological horizon, the lower bound for the grey-body factor becomes

$$T \geq T_b = \mathrm{sech}^2\left(\frac{1}{2\omega}\int_{r_H}^{\infty} \frac{|V|}{f(r)}\, dr\right) = \mathrm{sech}^2\left(\frac{A_l}{2\omega}\right), \tag{37}$$

where

$$A_l = \int_{r_H}^{\infty} \left|\frac{l(l+1)}{r^2} + \frac{f'}{r}\right| dr, \tag{38}$$

and r_H denotes the event horizon (outer horizon).

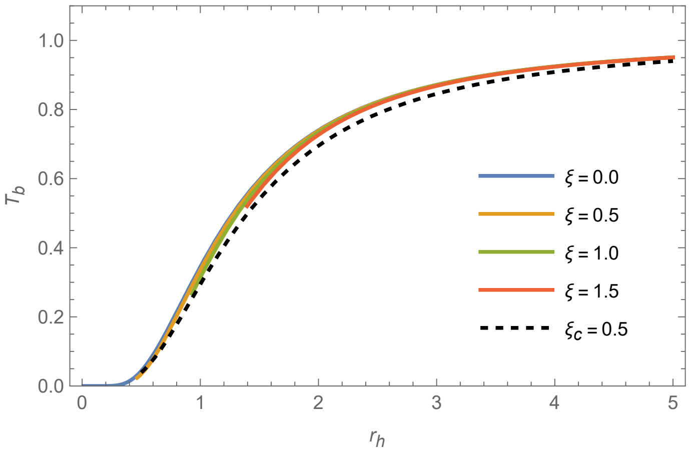

Figure 8. Lower bound for the grey-body factor T_b as a function of the event horizon radius r_h. The solid curves represent the RG-improved Schwarzschild black hole in Scheme-B for different values of the cutoff scale parameter ξ. The dashed black curve corresponds to the regularization Scheme-C for $\xi = 0.5$. Remaining parameters: $l = 1$ and $\omega = 1.0$. All curves asymptotically recover the classical Schwarzschild behavior, $T_b \to 1$, in the limit $r_h \to \infty$. The domain of each curve is restricted to the physical region $r_h \geq r_{\text{rem}}$, where $r^B_{\text{rem}} = (3/4)^{1/4}\xi$ and $r^C_{\text{rem}} = \xi$, representing the formation of a cold remnant at $T_H = 0$.

The numerical results for the lower bound of the grey-body factor T_b, shown in Figure 8, reveal that quantum corrections significantly modify the emission transparency of the black hole. For all cases, T_b increases with the horizon radius r_h, starting from a non-zero value at the remnant radius and asymptotically reaching the Schwarzschild limit ($T_b \to 1$) for large r_h.Comparing the two regularization schemes, Scheme-C consistently yields lower grey-body factors than Scheme-B for a fixed ξ. This indicates that the geometry in Scheme-C produces a more reflective potential barrier, resulting in a larger opacity A_l as defined in Equation (38), which suppresses the transmission probability. Regarding the influence of the cutoff scale in the the black hole metric (Scheme-B), we observe that higher values of ξ lead to a decrease in T_b. Physically, an increase in the parameter ξ enhances the quantum gravity effects near the origin, which effectively increases the spacetime opacity. Consequently, the potential barrier becomes more efficient at filtering outgoing radiation, reducing the grey-body factor across the physical range of r_h.

The fact that T_b does not vanish at the remnant radius, despite the Hawking temperature T_H being zero, indicates that the quantum-corrected geometry remains partially transparent to radiation even in the cold remnant limit, a feature that distinguishes these RG-improved models from the classical case.

7. Shadow Analysis and Observational Constraints

The shadow of a black hole is a critical observable that provides a direct signature of the underlying spacetime geometry near the event horizon. For a static and spherically symmetric metric of the form 5, the shadow's boundary is determined by the existence of unstable circular photon orbits. The radius of the photon sphere, r_{ph}, is obtained by finding the largest root of the equation

$$r_{ph} f'(r_{ph}) - 2f(r_{ph}) = 0, \tag{39}$$

where the lapse function $f(r)$ is defined according to the specific regularization scheme under consideration. For Scheme-B, we employ Equation (6), while for the reference Scheme-C, we use Equation (7). An observer at an asymptotic distance from the black hole perceives a shadow with a radius R_{sh} that is geometrically magnified by gravitational lensing. This observed radius is defined by the critical impact parameter given by

$$R_{sh} = r_{ph}/\sqrt{f(r_{ph})}, \tag{40}$$

which depends on the specific value of the scale parameter ξ. In the classical limit where $\xi \to 0$, both regularization schemes recover the standard Schwarzschild result $R_{sh} = 3\sqrt{3}M \approx 5.196M$. As ξ

doi:10.20944/preprints202602.1300.v1

increases, the gravitational coupling $G(r)$ decreases due to the asymptotic safety corrections, leading to a weaker effective gravitational attraction. Consequently, the photon sphere and the resulting shadow radius exhibit a monotonic decrease as the quantum scale becomes more prominent.

Figure 9 displays the evolution of the shadow radius ratio R_{sh}/M compared against the 1σ observational bounds from the Event Horizon Telescope (EHT) for M87* (5.5 ± 0.85) and Sgr A* (4.8 ± 0.5). The horizontal bands illustrate the regions of observational consistency, with the central light-green region highlighting the overlapping confidence interval between both sources. Our results show that Scheme-B (solid blue line) is phenomenologically more robust than Scheme-C (dashed red line), as it predicts a more gradual decrease in the shadow size. While Scheme-C quickly reaches the lower bounds of the Sgr A* observations for small values of ξ/M, Scheme-B remains well within the overlapping experimental region for a significantly broader range of the regularization parameter. This suggests that the proposed black hole metric in Scheme-B provides a more stable description of astrophysical black holes under quantum gravity corrections.

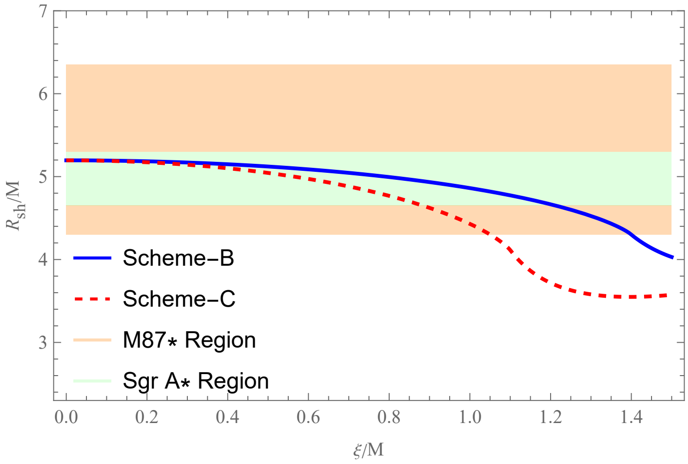

Figure 9. Shadow radius ratio R_{sh}/M as a function of the scale parameter ξ/M for Scheme-B (solid blue) and Scheme-C (dashed red). The shaded orange and light-green horizontal bands represent the 1σ observational constraints from M87* and Sgr A* according to EHT observations. Both models recover the Schwarzschild limit $(3\sqrt{3})$ at $\xi = 0$.

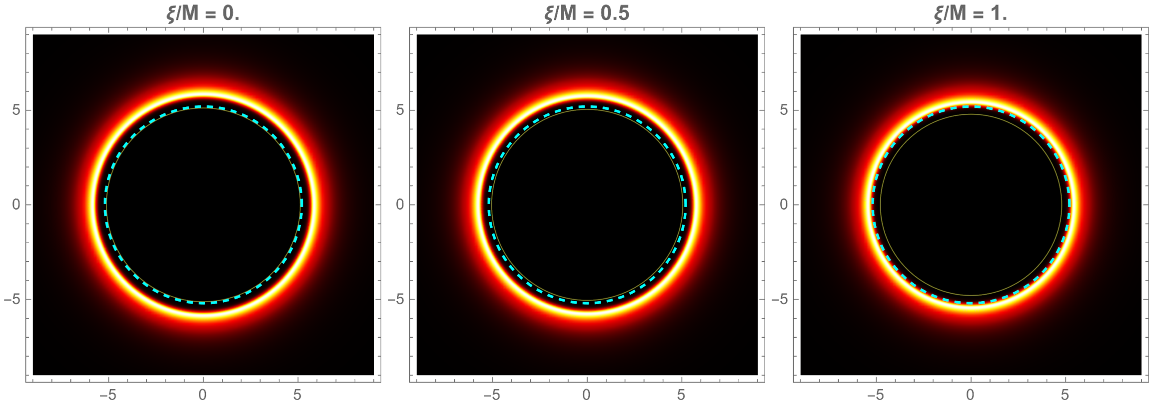

Figure 10. Intensity maps of the black hole shadow for different values of the ASG parameter ξ. The dark region corresponds to the critical impact parameter $b_c = R_{sh}$, the dashed blue circle marks the Schwarzschild reference radius, and the faint narrow ring near the boundary is associated with photons orbiting close to the photon sphere, with radius r_{ph}. The gradual decrease of the shadow size with increasing ξ reflects the effect of the quantum effects on photon trajectories.

doi:10.20944/preprints202602.1300.v1

In Figure 10, we present the visual rendering of the black hole shadows. To simulate the appearance of the accretion flow around the black hole, we implemented the Gralla–Lupsasca–Marrone (GLM) model described by the intensity profile given by

$$I(r,\mu,\sigma,\gamma) = \frac{\exp[-\frac{1}{2}(\gamma + \operatorname{arcsinh}((r-\mu)/\sigma))^2]}{\sqrt{(r-\mu)^2+\sigma^2}}. \tag{41}$$

The parameters μ, σ, and γ correspond to three distinct properties of the emission profile: The location of the central peak, its width, and its asymmetry, respectively [16,17]. In the resulting two-dimensional images, the peak emission parameter is set to $\mu = 1.35 r_{ph}$, effectively anchoring the maximum brightness near the photon ring to account for strong gravitational lensing and light pile-up at the critical curve. The width and asymmetry are controlled by $\sigma = M/6$ and $\gamma = -1.5$, respectively, providing a finite thickness and a smooth outward decay of the intensity. The dark circle corresponds to the central region where the impact parameter b is smaller than the critical value $b_c = R_{sh}$. Thus, the bright rings surrounding the shadows illustrate the emission from the accretion disk, where we intentionally emphasized the photon ring contribution to highlight the impact of the ξ parameter on the shadow's size and edge sharpness. As observed in the shadow plots, increasing the value of ξ leads to a progressive shrinkage of the shadow radius compared to the classical Schwarzschild limit, which is denoted by the dashed blue reference circles.

8. Conclusions

In this study, we investigated a new improved Schwarzschild black hole geometry originating from the Asymptotic Safety program, specifically focusing on the infrared (IR) limit of the renormalization group improvement. Employing Scheme-B for running Newtonian coupling according to [19], we analyzed a metric where the non-local scale ξ significantly modifies the horizon structure and the late-stage evaporation process. It is important to emphasize that, as an IR-limit model, this solution focuses on the macroscopic and intermediate-scale corrections; thus, it preserves the singular nature at the origin while introducing a fundamental departure from the classical Schwarzschild evolution.

A primary result of our analysis is the deviation from the usual black hole thermodynamics. In the classical scenario, a Schwarzschild black hole possesses a temperature that diverges as the mass vanishes, leading to an unstable and complete evaporation. In contrast, the Scheme-B geometry introduces a critical change: the Hawking temperature reaches a maximum and then drops to zero at a finite remnant radius $r_{rem} = (3/4)^{1/4}\xi$. This behavior indicates that the quantum-corrected black hole does not evaporate completely but instead stabilizes into a cold remnant after suffering a phase transition, confirmed by the behavior of the heat capacity and the Gibbs free energy.

The internal consistency of this extended thermodynamic picture was validated through the HPEM geometric formalism. The thermodynamic curvature scalar R^{HPEM} successfully mapped the phase space of the model, exhibiting a divergence at the remnant radius that marks the breakdown of the classical thermodynamic description. Furthermore, a second divergence in R^{HPEM} at larger radii identifies a second-order phase transition associated with the heat capacity's instability. These geometric features are perfectly aligned with the corrected entropy law, which incorporates universal logarithmic terms.

The thermodynamic consistency of the model was further reinforced by the topological analysis. By interpreting the on-shell states of the RG-improved Schwarzschild black hole as defect structures in an off-shell free-energy landscape, we constructed the phase-space vector field $\vec{\phi}(r_h, \Theta)$. We found that the physical domain is naturally bounded from below by the cold-remnant condition, since $T_H(r_{\rm rem}) = 0$ implies $\tau_H = 1/T_H \to \infty$ at the remnant radius. For any fixed $\tau > \tau_{\rm min}$, the equation $\tau = \tau_H(r_h)$ admits two solutions appearing as isolated zeros of $\vec{\phi}$ (typically carrying opposite winding numbers), encoding the two thermodynamic branches separated by the critical point, in agreement with the divergence observed in the heat capacity. Notably, although the defect pattern is topologically equivalent between Scheme-B and Scheme-C, the former yields a smoother deformation of the

Schwarzschild landscape, reinforcing the scenario of a regulated evaporation process that culminates in a stable remnant.

Complementing the equilibrium analysis, we investigated the propagation properties of massless scalar perturbations through the effective potential barrier via the grey-body factors. By deriving a lower bound for the transmission probability, $T \geq \text{sech}(A_l/2\omega)^2$, our numerical results showed that quantum corrections systematically modify the spacetime opacity. Specifically, the transmission probability T_b increases with the horizon radius, asymptotically recovering the Schwarzschild limit $T_b \to 1$, whereas increasing the non-local scale ξ suppresses T_b across the physical domain, indicating that ASG corrections enhance the effective barrier felt by outgoing modes. A comparison between the regularization prescriptions further reveals that Scheme-C produces a more reflective barrier than our proposed Scheme-B. Finally, we found that T_b remains non-zero at $r_h = r_{\text{rem}}$; this does not imply a non-vanishing Hawking flux, since $T_H(r_{\text{rem}}) = 0$, but rather indicates that the remnant spacetime retains partial transparency to external scalar perturbations, a distinctive imprint of asymptotic-safety corrections in the infrared regime.

Finally, the agreement between our predicted shadow radii and the EHT observations for $M87^*$ and Sgr A^* confirms that these IR modifications are not only theoretically consistent but also phenomenologically viable, providing a robust bridge between quantum gravity effects and observational astrophysics.

Acknowledgments: FBL is funded by Fundação Cearense de Apoio ao Desenvolvimento Científico e Tecnológico (FUNCAP) and by Conselho Nacional de Desenvolvimento Científico e Tecnológico (CNPq), grant number 305947/2024-9. CRM is funded by Conselho Nacional de Desenvolvimento Científico e Tecnológico (CNPq), under the grant 308268/2021-6.

References

1. Batista, A.; et al. White paper and roadmap for quantum gravity phenomenology in the multi-messenger era. *Class. and Quantum Grav.* **2025**, *42*, 032001, [arXiv:gr-qc/2312.00409]. https://doi.org/10.1088/1361-6382/ad605a.
2. Bekenstein, J.D. Black holes and the second law. *Lettere al Nuovo Cimento (1971-1985)* **1972**, *4*, 737–740. https://doi.org/10.1007/BF02757029.
3. Hawking, S.W. Black hole explosions? *Nature* **1974**, *248*, 30–31. https://doi.org/10.1038/248030a0.
4. Hawking, S.W.; Page, D.N. Thermodynamics of black holes in anti-de Sitter space. *Commun. Math. Phys.* **1983**, *87*, 577–588. https://doi.org/10.1007/BF01208266.
5. Carlip, S. Entropy from conformal field theory at Killing horizons. *Classical and Quantum Gravity* **1999**, *16*, 3327. https://doi.org/10.1088/0264-9381/16/10/322.
6. Maldacena, J., The AdS/CFT Correspondence. In *Handbook of Quantum Gravity*; Bambi, C.; Modesto, L.; Shapiro, I., Eds.; Springer Nature Singapore: Singapore, 2023; pp. 1–24. https://doi.org/10.1007/978-981-19-3079-9_65-1.
7. Amelino-Camelia, G. Quantum-Spacetime Phenomenology. *Living Rev. Relativ.* **2013**, *16*, 5. https://doi.org/10.12942/lrr-2013-5.
8. Abbott, R.; et al. GWTC-2: Compact Binary Coalescences Observed by LIGO and Virgo During the First Half of the Third Observing Run. *Phys. Rev. X* **2021**, *11*, 021053, [arXiv:gr-qc/2010.14527]. https://doi.org/10.1103/PhysRevX.11.021053.
9. Agazie, G.; et al. The NANOGrav 15 yr Data Set: Constraints on Supermassive Black Hole Binaries from the Gravitational-wave Background. *apjl* **2023**, *952*, L37, [arXiv:astro-ph.HE/2306.16220]. https://doi.org/10.3847/2041-8213/ace18b.
10. Akiyama, K.; et al. First Sagittarius A* Event Horizon Telescope Results. I. The Shadow of the Supermassive Black Hole in the Center of the Milky Way. *Astrophys. J. Lett.* **2022**, *930*, L12, [arXiv:astro-ph.HE/2311.08680]. https://doi.org/10.3847/2041-8213/ac6674.
11. Abac, A.G.; et al. GW250114: Testing Hawking's Area Law and the Kerr Nature of Black Holes. *Phys. Rev. Lett.* **2025**, *135*, 111403. https://doi.org/10.1103/kw5g-d732.

12. Bambi, C.; Barausse, E. CONSTRAINING THE QUADRUPOLE MOMENT OF STELLAR-MASS BLACK HOLE CANDIDATES WITH THE CONTINUUM FITTING METHOD. *The Astrophysical Journal* **2011**, *731*, 121. https://doi.org/10.1088/0004-637X/731/2/121.
13. Cunha, P.V.P.; Herdeiro, C.A.R. Shadows and strong gravitational lensing: a brief review. *General Relativity and Gravitation* **2018**, *50*, 42. https://doi.org/10.1007/s10714-018-2361-9.
14. Vagnozzi, S.; et al. Horizon-scale tests of gravity theories and fundamental physics from the Event Horizon Telescope image of Sagittarius A. *Class. Quant. Grav.* **2023**, *40*, 165007, [arXiv:gr-qc/2205.07787]. https://doi.org/10.1088/1361-6382/acd97b.
15. Vagnozzi, S.; Roy, R.; Tsai, Y.D.; Visinelli, L.; Afrin, M.; Allahyari, A.; Bambhaniya, P.; Dey, D.; Ghosh, S.G.; Joshi, P.S.; et al. Horizon-scale tests of gravity theories and fundamental physics from the Event Horizon Telescope image of Sagittarius A^*. *Classical and Quantum Gravity* **2023**, *40*, 165007. https://doi.org/10.1088/1361-6382/acd97b.
16. Gralla, S.E.; Lupsasca, A.; Marrone, D.P. The shape of the black hole photon ring: A precise test of strong-field general relativity. *Phys. Rev. D* **2020**, *102*, 124004, [arXiv:gr-qc/2008.03879]. https://doi.org/10.1103/PhysRevD.102.124004.
17. Vincent, F.H.; Gralla, S.E.; Lupsasca, A.; Wielgus, M. Images and photon ring signatures of thick disks around black holes. *Astron. Astrophys.* **2022**, *667*, A170, [arXiv:astro-ph.HE/2206.12066]. https://doi.org/10.1051/0004-6361/202244339.
18. Muniz, C.R.; Lustosa, F.B.; Tangphati, T. Einstein-Yang-Mills Regular Black Holes in Rainbow Gravity. *General Relativity and Gravitation* **2025**, *57*, 125. https://doi.org/10.1007/s10714-025-03458-2.
19. Bonanno, A.M.; Konoplya, R.A.; Oglialoro, G.; Spina, A. Regular black holes from proper-time flow in quantum gravity and their quasinormal modes, shadow and Hawking radiation. *Journal of Cosmology and Astroparticle Physics* **2025**, *2025*, 042. https://doi.org/10.1088/1475-7516/2025/12/042.
20. Platania, A., Black Holes in Asymptotically Safe Gravity. In *Handbook of Quantum Gravity*; Bambi, C.; Modesto, L.; Shapiro, I., Eds.; Springer Nature Singapore: Singapore, 2024; pp. 1031–1095. https://doi.org/10.1007/978-981-99-7681-2_24.
21. Reuter, M. Nonperturbative evolution equation for quantum gravity. *Phys. Rev. D* **1998**, *57*, 971–985. https://doi.org/10.1103/PhysRevD.57.971.
22. Niedermaier, M. The asymptotic safety scenario in quantum gravity: an introduction. *Classical and Quantum Gravity* **2007**, *24*, R171. https://doi.org/10.1088/0264-9381/24/18/R01.
23. Anber, M.M.; Donoghue, J.F. Running of the gravitational constant. *Phys. Rev. D* **2012**, *85*, 104016, [arXiv:hep-th/1111.2875]. https://doi.org/10.1103/PhysRevD.85.104016.
24. Weinberg, S. Asymptotically safe inflation. *Phys. Rev. D* **2010**, *81*, 083535. https://doi.org/10.1103/PhysRevD.81.083535.
25. Bonanno, A.; Reuter, M. Renormalization group improved black hole spacetimes. *Phys. Rev. D* **2000**, *62*, 043008. https://doi.org/10.1103/PhysRevD.62.043008.
26. Moti, R.; Shojai, A. On the cutoff identification and the quantum improvement in asymptotically safe gravity. *Physics Letters B* **2019**, *793*, 313–319. https://doi.org/https://doi.org/10.1016/j.physletb.2019.04.062.
27. Stashko, O. Quasinormal modes and gray-body factors of regular black holes in asymptotically safe gravity. *Phys. Rev. D* **2024**, *110*, 084016. https://doi.org/10.1103/PhysRevD.110.084016.
28. Bonanno, A.; Oglialoro, G.; Zappalà, D. Gauge and parametrization dependence of quantum Einstein gravity within the proper time flow. *Phys. Rev. D* **2025**, *112*, 026002. https://doi.org/10.1103/sht5-sf25.
29. Hendi, S.H.; Panahiyan, S.; Eslam Panah, B.; Momennia, M. A new approach toward geometrical concept of black hole thermodynamics. *Eur. Phys. J. C* **2015**, *75*, 507, [arXiv:gr-qc/1506.08092]. https://doi.org/10.1140/epjc/s10052-015-3701-5.
30. Soroushfar, S.; Upadhyay, S. Phase transition of a charged AdS black hole with a global monopole through geometrical thermodynamics. *Phys. Lett. B* **2020**, *804*, 135360, [arXiv:gr-qc/2003.06714]. https://doi.org/10.1016/j.physletb.2020.135360.
31. Chabab, M.; Iraoui, S. Thermodynamic criticality of d-dimensional charged AdS black holes surrounded by quintessence with a cloud of strings background. *Gen. Rel. Grav.* **2020**, *52*, 75, [arXiv:hep-th/2001.06063]. https://doi.org/10.1007/s10714-020-02729-4.
32. Wei, S.W.; Liu, Y.X.; Mann, R.B. Black hole solutions as topological thermodynamic defects. *Physical Review Letters* **2022**, *129*, 191101.
33. Page, D.N. Particle emission rates from a black hole: Massless particles from an uncharged, nonrotating hole. *Phys. Rev. D* **1976**, *13*, 198–206. https://doi.org/10.1103/PhysRevD.13.198.

34. Al-Badawi, A. Greybody factors emitted by a regular black hole in a non-minimally coupled Einstein-Yang-Mills theory. *The European Physical Journal C* **2023**, *83*, 380. https://doi.org/10.1140/epjc/s10052-023-11550-7.
35. Sekhmani, Y.; Maurya, S.; Rayimbaev, J.; Altanji, M.; Ibragimov, I.; Muminov, S. Black hole quasinormal modes, greybody factors and quasi-periodic oscillations in teleparallel Born-Infeld gravity. *Nuclear Physics B* **2025**, *1021*, 117210. https://doi.org/https://doi.org/10.1016/j.nuclphysb.2025.117210.
36. Boonserm, P.; Ngampitipan, T.; Wongjun, P. Greybody factor for black string in dRGT massive gravity. *The European Physical Journal C* **2019**, *79*, 330. https://doi.org/10.1140/epjc/s10052-019-6827-z.
37. Oshita, N. Greybody factors imprinted on black hole ringdowns: An alternative to superposed quasinormal modes. *Phys. Rev. D* **2024**, *109*, 104028. https://doi.org/10.1103/PhysRevD.109.104028.